# Anomalies in bulk supercooled water at negative pressure

Gaël Pallares[a], Mouna El Mekki Azouzi[a], Miguel A. González[b], Juan L. Aragones[b], José L. F. Abascal[b], Chantal Valeriani[b], and Frédéric Caupin[a,1]

[a]Institut Lumière Matière, Unité Mixte de Recherche 5306 Université Lyon 1, Centre National de la Recherche Scientifique, Université de Lyon and Institut Universitaire de France, 69622 Villeurbanne Cedex, France; and [b]Departamento de Química Física I, Facultad de Ciencias Químicas, Universidad Complutense de Madrid, 28040 Madrid, Spain

Edited by Pablo G. Debenedetti, Princeton University, Princeton, NJ, and approved April 11, 2014 (received for review December 17, 2013)

**Water anomalies still defy explanation. In the supercooled liquid, many quantities, for example heat capacity and isothermal compressibility $\kappa_T$, show a large increase. The question arises if these quantities diverge, or if they go through a maximum. The answer is key to our understanding of water anomalies. However, it has remained elusive in experiments because crystallization always occurred before any extremum is reached. Here we report measurements of the sound velocity of water in a scarcely explored region of the phase diagram, where water is both supercooled and at negative pressure. We find several anomalies: maxima in the adiabatic compressibility and nonmonotonic density dependence of the sound velocity, in contrast with a standard extrapolation of the equation of state. This is reminiscent of the behavior of supercritical fluids. To support this interpretation, we have performed simulations with the 2005 revision of the transferable interaction potential with four points. Simulations and experiments are in near-quantitative agreement, suggesting the existence of a line of maxima in $\kappa_T$ (LM$\kappa_T$). This LM$\kappa_T$ could either be the thermodynamic consequence of the line of density maxima of water [Sastry S, Debenedetti PG, Sciortino F, Stanley HE (1996) *Phys Rev E* 53:6144–6154], or emanate from a critical point terminating a liquid–liquid transition [Sciortino F, Poole PH, Essmann U, Stanley HE (1997) *Phys Rev E* 55:727–737]. At positive pressure, the LM$\kappa_T$ has escaped observation because it lies in the "no man's land" beyond the homogeneous crystallization line. We propose that the LM$\kappa_T$ emerges from the no man's land at negative pressure.**

scenarios for water | Widom line | Berthelot tube

Water differs in many ways from standard liquids: ice floats on water, and, upon cooling below 4°C, the liquid density decreases. In the supercooled liquid, many quantities, for example heat capacity and isothermal compressibility, show a large increase. Extrapolation of experimental data suggested a power-law divergence of these quantities at −45°C (1). Thirty years ago, the stability-limit conjecture proposed that an instability of the liquid would cause the divergence (2) (Fig. 1*A*). This is supported by equations of state (EoSs), such as the International Association for the Properties of Water and Steam (IAPWS) EoS (3), fitted on the stable liquid and extrapolated to the metastable regions. Ten years later, the second critical point interpretation, based on simulations (4), proposed that, instead of diverging, the anomalous quantities would reach a peak, near a Widom line (5, 6) that emanates from a liquid–liquid critical point (LLCP) terminating a first-order liquid–liquid transition (LLT) between two distinct liquid phases at low temperature (Fig. 1*B*). The two scenarios differ in the shape of the line of density maxima (LDM) of water (Fig. 1 *A* and *B*). A recent work (7) has added one point on this line at large negative pressure, but this was not enough to decide between the two scenarios.

It has been argued (8) that the stability-limit conjecture would imply the existence of an improbable second, low-temperature liquid–vapor critical point. However, it is not necessary if the line of instability at positive pressure is not a liquid–vapor spinodal, but rather a line of instability toward another phase. The critical-point free scenario (9–11) (Fig. 1*C*) provides such a line. There would be an LLT, but its critical point would be absent because it lies beyond the liquid–vapor spinodal. The low-density liquid could become metastable at low temperature, but unstable on the liquid–liquid spinodal, where $\kappa_T$ would diverge. Finally, the singularity-free scenario (12) (Fig. 1*D*) does not exhibit any LLT. It predicts peaks in several thermodynamic quantities instead of divergences, which would be "the thermodynamically inevitable consequences of the existence of density anomalies" (8). It may also be seen as a second critical-point interpretation, but with an LLCP at zero temperature (11, 13).

In bulk water at positive pressure, despite tremendous efforts (8) decisive experiments to discriminate between the proposed scenarios have been precluded by unavoidable crystallization. To circumvent this problem, water proxies have been used: water confined in narrow pores (14), or bulk water–glycerol mixtures (15). Although the results supported the second critical-point interpretation, their relevance to bulk water is not straightforward.

Here we study bulk water samples, a few micrometers in diameter, in the doubly metastable region: the liquid is simultaneously supercooled and exposed to mechanical tension or negative pressure. Negative pressures occur in nature, e.g., in the sap of trees, under the tentacles of octopi, or in fluid inclusions in minerals (16, 17). The study of the largest tensions achievable in water was pioneered by the group of Angell (18). They used

## Significance

**Water is the most familiar liquid, and arguably the most complex. Anomalies of supercooled water have been measured during decades, and competing interpretations proposed. Yet, a decisive experiment remains elusive, because of unavoidable crystallization into ice. We investigate the state of water that is both supercooled and under mechanical tension, or negative pressure. Liquids under negative pressure can be found in plants or fluid inclusions in minerals. Using such water inclusions in quartz, we report, to our knowledge, the first measurements on doubly metastable water down to −15°C and around −100 MPa. We observe sound velocity anomalies that can be reproduced quantitatively with molecular dynamics simulations. These results suggest the possibility to rule out two proposed scenarios for water anomalies, and put further constraints on the remaining ones.**

Author contributions: F.C. designed research; G.P., M.E.M.A., and M.A.G. performed research; G.P., M.A.G., J.L.A., J.L.F.A., C.V., and F.C. analyzed data; M.E.M.A. selected the inclusions; and J.L.F.A., C.V., and F.C. wrote the paper.

The authors declare no conflict of interest.

This article is a PNAS Direct Submission.

[1]To whom correspondence should be addressed. E-mail: frederic.caupin@univ-lyon1.fr.

This article contains supporting information online at www.pnas.org/lookup/suppl/doi:10.1073/pnas.1323366111/-/DCSupplemental.

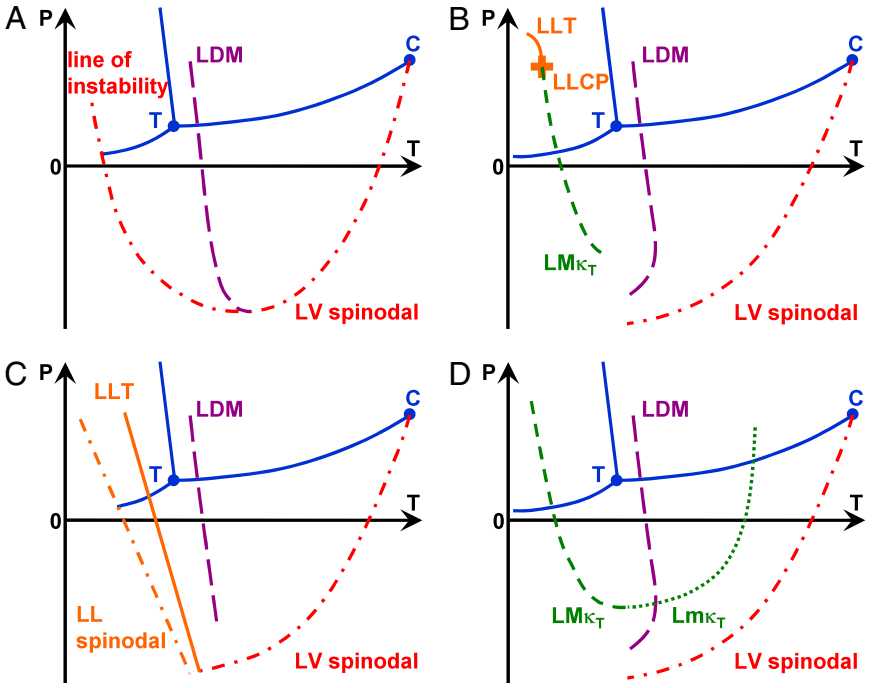


**Fig. 1.** Scenarios proposed to explain water anomalies. Schematic phase diagrams for water in the pressure–temperature plane with equilibrium transitions between liquid, vapor, and ice (solid blue curves); T is the triple point and C the liquid–vapor critical point. (*A*) Stability-limit conjecture (2). If the LDM (long-dashed purple curve) reaches the liquid–vapor (LV) spinodal (dashed-dotted red curve) at negative pressure, the latter bends to lower tension at lower temperature. This would provide a line of instability at positive pressure on which several thermodynamic functions would diverge. (*B*) Second critical-point scenario (4). The LDM bends to lower temperatures at larger tension, and the LV spinodal remains monotonic. The anomalies of supercooled water are due to the vicinity of an LLCP terminating an LLT (solid orange curve). Thermodynamic functions exhibit a peak on lines emanating from the LLCP (5, 6), such as the line of isothermal compressibility maxima along isobars ($LM\kappa_T$, short-dashed green curve). (*C*) Critical-point free scenario (9–11). The LLT extends down to the LV spinodal, so that there is no accessible LLCP. The spinodal associated with the LLT (LL spinodal, dashed-dotted orange curve) would cause the divergence of several thermodynamic functions. (*D*) Singularity-free interpretation (12). There is no LLT or LLCP. Thermodynamic functions do not diverge, but several exhibit extrema as a consequence of the existence of an LDM. The LDM reaches its highest temperature when it crosses one of the lines of isothermal compressibility extrema along isobars; the case where it is the line of minima ($Lm\kappa_T$, dotted green curve) is displayed.

a "Berthelot tube" technique (Fig. 2*A*), based on isochoric cooling of a micrometer-size inclusion of water in quartz. Tensions as large as −140 MPa have been reported, and confirmed by others (7, 19, 20), which exceed by far the limit of other techniques (16, 17). It was already recognized in the work of Angell that the high-density water inclusions that were able to survive cooling to room temperature without cavitation were also able to be supercooled below 0°C. Indeed, when the isochore crosses the LDM of water, the tension is released and cavitation becomes less likely. Another study (21) using macroscopic Berthelot tubes also reached the doubly metastable region, but the tensions were around −10 MPa only.

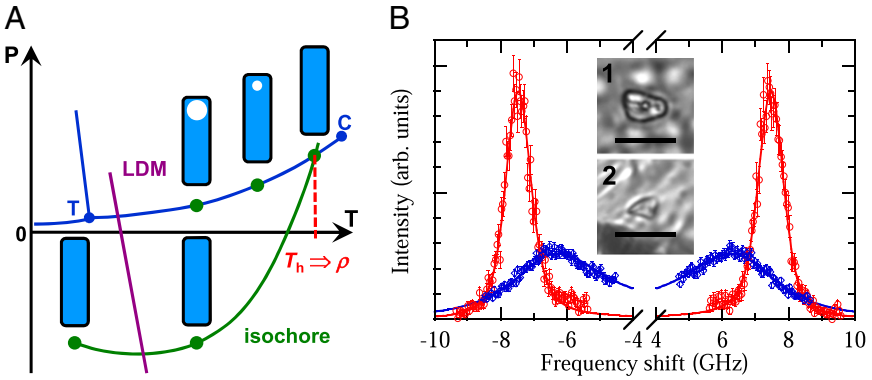


**Fig. 2.** Experiments on metastable liquid water. (*A*) Berthelot tube method (7, 18–20). A closed, rigid container with a fixed amount of water is heated until the last vapor bubble disappears at $T_h$. Upon cooling, the bubble does not reappear and the liquid follows an isochore (green curve) and is put under mechanical tension. If the density is high enough, cavitation does not occur and the liquid can reach the doubly metastable region, where water is both supercooled and under tension. (*B*) Typical Brillouin spectra. They were obtained with the homogenized sample 1 at 140°C (red circles) and −12°C (blue diamonds). The solid curves are fits used to obtain the sound velocity (*Materials and Methods*, *Brillouin Light Scattering*). Note that the −12°C spectrum was rescaled to the same exposure time as the 140°C spectrum for easier comparison. The samples are shown as inset (scale bars, 10 μm).

To reach large tensions, we use two microscopic inclusions of water in quartz (Fig. 2*B*, *Inset*) (*Materials and Methods*, *Samples*). We perform Brillouin light-scattering experiments on these samples; this technique gives access to the sound velocity within the liquid. Several Brillouin light-scattering studies on supercooled water at ambient pressure are available (22–27), but only two works investigated water under tension. One used fluid inclusions (19): all samples in that study cavitated above room temperature except one with a density close to that of our sample 1. However, measurements in ref. 19 were reported only down to 0°C, and the direct comparison with an extrapolated EoS was not considered. Another work (28) confirmed the validity of the extrapolation of the IAPWS EoS, but only at room temperature and down to −26 MPa. Our work extends the covered range to supercooled water under tension, reporting measurements down to −15°C along two isochores at $\rho_1 = 933.2 \pm 0.4$ kg m$^{-3}$ and $\rho_2 = 952.5 \pm 1.5$ kg m$^{-3}$, and reaching pressures beyond −100 MPa (*SI Text*).

## Results

Representative Brillouin spectra are shown in Fig. 2*B*. Such spectra are analyzed to give the zero-frequency sound velocity $c$ (*Materials and Methods*, *Brillouin Light Scattering*). To support the experimental results, we also perform molecular dynamics simulations of $c$. Previous numerical studies of water at negative pressure are available for several potentials: ST2 (4), SPC/E (29), and TIP5P (30). They all find a liquid–vapor spinodal whose pressure increases monotonically with temperature, and an LDM that avoids meeting the spinodal, in contrast with the stability-limit conjecture. Here we choose to use the 2005 revision of the transferable interaction potential with four points (TIP4P/2005) (31) because it has demonstrated an excellent overall performance (32) and, in particular, it yields results in satisfactory agreement with the reported experimental results in the supercooled region (33). Thus, we calculate values of $c$ for TIP4P/2005 at the experimental thermodynamic conditions (*Materials and Methods*, *Molecular Dynamics Simulations*).

Fig. 3 shows the experimentally measured and the numerically computed values of $c$ as a function of temperature at several thermodynamic conditions. Let us first describe the measurements on sample 1 after cavitation, at temperatures up to $T_{h,1}$: at these conditions the liquid is in equilibrium with its vapor. The measured sound velocity is in excellent agreement with the known sound velocity along the binodal and with our simulations of TIP4P/2005 water along its binodal (34). The agreement between simulations and tabulated experimental data also illustrates the quality of the potential used to simulate water (31). When the temperature of sample 1 reaches $T_{h,1}$, the last vapor bubble disappears, leaving the inclusion entirely filled with liquid at density $\rho_1$. Upon further heating, the pressure increases along the $\rho_1$ isochore. Once more, the measurements agree with the sound velocity from the known EoS and from our simulations along the $\rho_1$ isochore. Note that the measurements leave the binodal exactly at $T_{h,1}$, which has been determined independently by direct observation under the microscope. This consistency further corroborates the robustness of our data.

Next, we make sample 1 metastable by cooling along the $\rho_1$ isochore. We observe that below $T_{h,1}$, the measured sound velocity starts diverging with respect to the one extrapolated using the IAPWS EoS. In contrast, it agrees with our simulations. The IAPWS EoS predicts a reentrant liquid–vapor spinodal: In this case, one would expect the sound velocity curve to reach a small value when the isochore approaches the spinodal at low temperature (for $\rho_1$, the IAPWS EoS predicts that they meet at −15°C with $c = 697$ m s$^{-1}$). On the contrary, both experiment and simulation give a sound velocity that reaches a minimum near 0°C, before increasing on further cooling. Therefore, the isochore at $\rho_1$ does not approach the liquid–vapor spinodal as expected from the

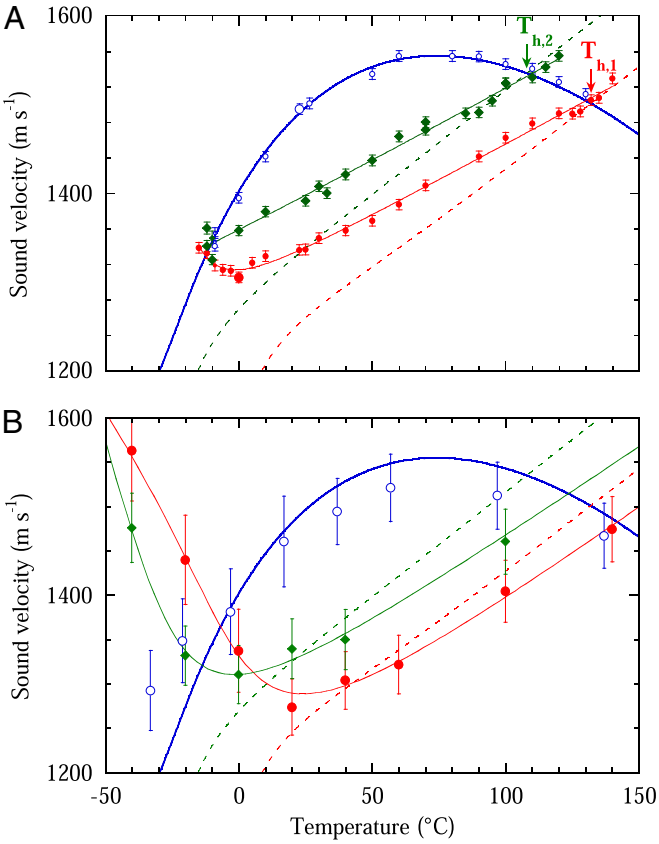


**Fig. 3.** Sound velocity as a function of temperature. The IAPWS EoS is used to plot the sound velocity along the binodal (thick blue curve) and along the isochores at $\rho_1$ (dashed red curve) and $\rho_2$ (dashed green curve). (*A*) Comparison with experiments. The symbols show our measurements on sample 1 after cavitation (open blue circles) and on metastable samples 1 (filled red circles) and 2 (filled green diamonds). The three symbol sizes correspond to three pinhole sizes on the spectrometer. The solid red and green curves are guides to the eye. The arrows show the homogenization temperatures of samples 1 and 2 as observed under the microscope. (*B*) Comparison with simulations of TIP4P/2005 water. The sound velocity was calculated along the TIP4P/2005 binodal (open blue circles), and the isochores at $\rho_1$ (filled red circles) and $\rho_2$ (filled green diamonds). The solid red and green curves are guides to the eye. Whereas the IAPWS EoS predicts a monotonic variation of $c$ along the isochores, both experiments and simulations find that $c$ reaches a minimum and increases above the values on the binodal at low temperature.

IAPWS EoS. The sound velocity $c$ is related to the adiabatic compressibility $\kappa_S$ through $c = 1/\sqrt{\rho\kappa_S}$, where $\rho$ is the density. Because we follow an isochore, the sound velocity minimum corresponds to a maximum in the adiabatic compressibility. Eventually, the sound velocity reaches a value higher than the value that one would expect along the binodal at −15°C, even though $\rho_1$ lies below the liquid density on the binodal, $\rho_0 = 996.3$ kg m$^{-3}$ at −15°C (35).

To confirm our results, we have repeated measurements and simulations on sample 2 with a higher density $\rho_2$. We find a similar deviation from the extrapolation of the IAPWS EoS. In the simulations, the sound velocity reaches a minimum, which is not clear in the experiments that seem to reach a plateau. This is consistent with the fact that the simulations find the minimum for $\rho_2$ at a temperature lower than for $\rho_1$, whereas for $\rho_1$ the experiment finds the minimum at a temperature lower than the simulations. Therefore, it is likely that the minimum for $\rho_2$ lies at temperatures below the one reached in the experiment. In both experiment and simulations, whereas at −12°C $\rho_2$ is between $\rho_1$ and $\rho_0$, the corresponding sound velocity is even slightly higher than both. Therefore, the sound velocity must reach a minimum

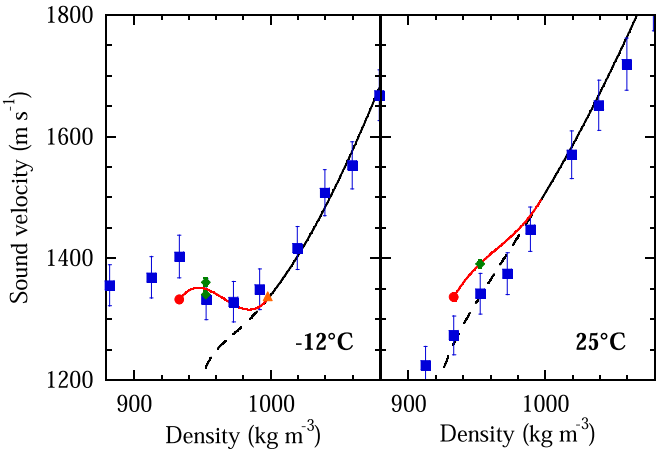


**Fig. 4.** Sound velocity versus density at −12°C and 25°C. The IAPWS EoS is shown in black, as a solid curve above the binodal, and as a dashed curve for its extrapolation to lower density. Our measurements for $\rho_1$ and $\rho_2$ are shown as filled red circles and green diamonds, respectively. The red curves are guides to the eye chosen to connect the data to the IAPWS EoS above the binodal with the correct slope. Note that the IAPWS EoS reproduces accurately experimental data above the binodal for stable water (e.g., at 25°C), and data along the binodal for supercooled water (e.g., at −12°C). To illustrate the latter, we have included (*Left*) the experimental value of the sound velocity at −11.2°C (orange triangle) from ref. 26. The solid blue squares give the results of the simulations of TIP4P/2005 water; note that the simulations (*Right*) were obtained at 20°C. At high temperature, measurements and simulations agree with the IAPWS EoS, whereas at low temperature, they suggest the occurrence of a minimum and maximum which are absent from the extrapolation of the IAPWS EoS.

between $\rho_2$ and $\rho_0$ along the −12°C isotherm. This is more clearly seen in Fig. 4: The sound velocity at $\rho_0$, $\rho_1$, and $\rho_2$ virtually falls on a horizontal line, but the slope of $c(\rho)$ at $\rho_0$ necessarily implies a minimum. This observation agrees with the predictions of the simulations but contrasts those of the IAPWS EoS.

## Discussion

To explain the observed anomalies, it is interesting to look for other systems with a minimum in $c(\rho)$ along an isotherm. This actually occurs in all fluids, in their supercritical phase: The sound velocity at a constant temperature above the liquid–vapor critical temperature passes through a minimum at a density close to the critical density (see for instance figure 8 of ref. 36 for methanol and ethanol). Based on this observation, we propose that the anomalies of the sound velocity, observed both in experiments and in simulations, are a signature of supercritical phenomena. Here, in addition, the sound velocity reaches a maximum when the density decreases (Fig. 4). This is because eventually the liquid–vapor spinodal density has to be reached, and then the sound velocity has to become small. A microscopic cell model (13) is able, by tuning two parameters, to reproduce each of the possible scenarios shown in Fig. 1. It should be interesting to investigate the behavior of the sound velocity within this model but this lies outside the scope of this work. It seems more convenient to use instead more realistic water models as a guide to better understand the origin of such anomalies. Several potentials predict an LLT in the supercooled region, ending at an LLCP. Based on the locus of maxima of $\kappa_T$ along isobars, an LLCP for TIP4P/2005 has been proposed at $T_c = 193$ K, $P_c = 135$ MPa, and $\rho_c = 1{,}012$ kg m$^{-3}$ (37), although the existence of an LLT for TIP4P/2005 is disputed in a recent paper (38). The LLCP is an appealing idea because it would give a reason for which water above 193 K behaves like a supercritical fluid.

One may wonder why all previous experiments at positive pressure failed to detect a peak in thermodynamic functions. Simulations with an LLT show that specific quantities (such as isothermal compressibility $\kappa_T$ or isobaric heat capacity) reach a peak on different lines, but that these lines all come close to each other near the LLCP, approaching asymptotically the locus of correlation length maxima, called the Widom line (6). The locus of maxima for $\kappa_T$ along isobars (LM$\kappa_T$) has been recently computed for TIP4P/2005 water at positive pressure (37). We have now computed this line also at negative pressure (*Materials and Methods*, *Molecular Dynamics Simulations*). The results are shown in Fig. 5 and compared with the isochores we studied and with the experimental line of homogeneous crystallization (39). At positive pressure, the LM$\kappa_T$ is not accessible to experiments because it lies in the so-called no man's land (40), a region where bulk liquid water cannot be observed experimentally. However, at negative pressure, the slope of the LM$\kappa_T$ becomes less negative than that of the line of homogeneous crystallization. Because the latter keeps the same slope, the LM$\kappa_T$ line leaves the no man's land and enters the doubly metastable region that we have now shown is accessible to quantitative experimentation.

Is there a way to directly observe the LLT? If it exists, it is likely to lie in the no man's land. Therefore, it will be hard to decide between the second critical-point interpretation (4) and the singularity-free scenario (12); note however that the latter can be seen (13) as an LLT with a critical point at 0 K. What our results do show is that the liquid–vapor spinodal does not reach the location predicted by extrapolation from the IAPWS EoS, and that the measured sound velocity quantitatively agrees with the one obtained with simulations of TIP4P/2005 water. This suggests that the sound velocity anomalies observed in the experiment are due to an LM$\kappa_T$, a feature present in the LLCP and singularity-free scenarios (Fig. 1 *B* and *D*), but absent from the stability limit conjecture and the critical-point free scenario (Fig. 1 *A* and *C*). The doubly metastable region therefore appears to

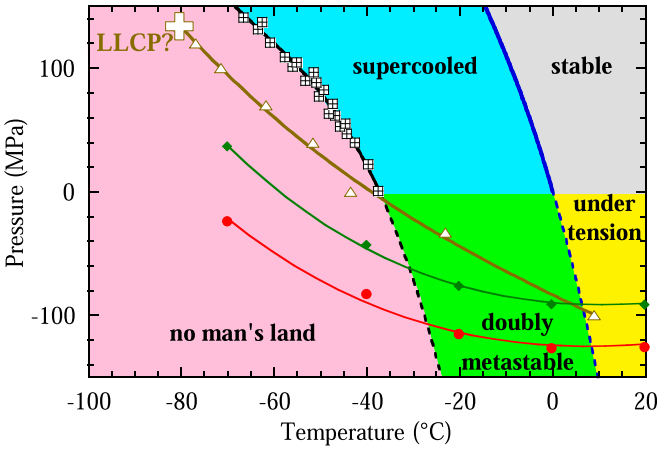


**Fig. 5.** Pressure–temperature phase diagram of water. Colored areas are used to identify the different possible states for liquid water. The melting line of ice Ih is shown at positive pressure by a solid blue curve and its extrapolation to negative pressure by a dashed blue curve. The black crossed squares show the experimental supercooling limit (39). They define the experimental homogeneous nucleation line (solid black curve), which is extrapolated here to negative pressure (dashed black curve). The $\rho_1$ and $\rho_2$ isochores of TIP4P/2005 water (see values in Tables S1 and S2) are shown by the red circles and curve, and green diamonds and curve, respectively. Simulations of TIP4P/2005 water are performed to find the maximum $\kappa_T$ along several isobars (white triangles), defining the LM$\kappa_T$ (brown curve), that might emanate from an LLCP (white plus symbol). Because the predictions of TIP4P/2005 are in satisfactory agreement with the reported experimental results in the supercooled region (33), this figure seems to indicate that the LM$\kappa_T$ (and other extrema in the response functions) might be accessible to experiment only in the doubly metastable region.

be a promising experimental territory to test other predictions from the models proposed to explain water anomalies.

## Materials and Methods

**Samples.** Sample 1 was prepared by hydrothermal synthesis (20); sample 2 is a natural sample from the French Alps, filled with meteoric water (Fig. 2*B*, *Inset*). The purity of water is estimated to be greater than 99.8 mol % (*SI Text*). The samples were placed on a heating–cooling stage (Linkam THMS 600) mounted on a microscope (Zeiss Axio Imager Vario). Phase changes in the inclusions were observed with a 100× Mitutoyo plan apo infinity-corrected long-working-distance objective. When a bubble is present in a sample, we observe its disappearance upon heating along the liquid–vapor equilibrium at the homogenization temperature: $T_{h,1} = 131.9 \pm 0.5$°C for sample 1 and $T_{h,2} = 107.9 \pm 2$°C for sample 2, where the numbers give the average and SD over a series of at least five measurements. The known data for the binodal (41) give the densities of water after homogenization: $\rho_1 = 933.2 \pm 0.4$ kg m$^{-3}$ and $\rho_2 = 952.5 \pm 1.5$ kg m$^{-3}$, respectively.

**Brillouin Light Scattering.** Brillouin scattering experiments were performed in backscattering geometry through the microscope objective. The sample is illuminated with a single longitudinal monomode laser (Coherent, Verdi V6) of wavelength $\lambda = 532$ nm focused to a 1-μm spot. The light scattered from the sample is collected on the entrance pinhole of a tandem Fabry–Perot interferometer (JRS Scientific, TFP-1). We use the recommended combination between entrance and output pinholes, and three different values for the entrance pinhole diameter: 150, 200, and 300 μm. A smaller pinhole gives less signal, but more resolution. It also reduces the volume of the sample from which the scattered light is allowed to enter the spectrometer, thus decreasing the parasitic light due to elastic scattering from the quartz crystal. Fig. 3*A* shows that the results are consistent for the three pinhole sizes used, indicating that the resolution is sufficient and validating the assumption that the elastically scattered light can be neglected in the analysis. Consequently we have fitted the Brillouin peaks only, using a viscoelastic model described in detail in ref. 42. It introduces a memory function with an exponential decay:

$$m(Q,t) = (c_\infty^2 - c^2)Q^2 \exp\left[-\left(\frac{c}{c_\infty}\right)^2 \frac{t}{\tau}\right], \quad [1]$$

where $Q$ is the wavevector probed by the scattering setup, $c$ and $c_\infty$ the sound velocity at zero and infinite frequency, respectively, and $\tau$ a structural relaxation time. $Q = 4\pi n/\lambda$, where $n$ is the refractive index of the liquid. In their Brillouin study, Alvarenga et al. (19) used for each isochore a constant value of $n$, determined from the known value at the homogenization temperature $T_h$. We chose instead to use a semiempirical formula based on the Lorentz–Lorenz relation (43). Along the liquid–vapor equilibrium line, it reproduces accurately the literature data. Note however that the difference with Alvarenga et al. is minimal: in the temperature range investigated, $n$ is almost constant along an isochore, varying from 1.31152 to 1.31456 for sample 1 and from 1.3184 to 1.321 for sample 2. The ratio between dynamic $(S(Q,\omega))$ and static $(S(Q))$ structure factor is

$$\frac{S(Q,\omega)}{S(Q)} = \frac{1}{\pi} \frac{(c\,Q)^2 m_R(Q,\omega)}{\left[\omega^2 - (c\,Q)^2 - \omega\, m_I(Q,\omega)\right]^2 + [\omega\, m_R(Q,\omega)]^2}, \quad [2]$$

where $m_R(Q,\omega)$ and $m_I(Q,\omega)$ are the real and imaginary parts of the Fourier transform of $m(Q,t)$, respectively.

To complete the analysis, the instrumental resolution function (IRF) and the dark count of the setup are needed. The IRF was determined for each pinhole from the elastically scattered light from a 10-mg L$^{-1}$ solution of milk in water, and well represented by a Gaussian. The dark count of the photodetector was also taken into account. It was determined from spectra taken with the spectrometer entrance closed, or with no signal reaching the entrance pinhole. The background was deduced from the dark count and the duration of each spectra, and its effect on the sound velocity is less than the 6-m s$^{-1}$ error bar on $c$ (*SI Text*).

We have then analyzed the spectra as follows. We take the functional form of the viscoelastic model (Eq. **2**), make a numerical convolution with the IRF, add the known dark count of the photomultiplier, and fit the resulting function on the raw spectra. We use three fitting parameters: $c$, $\tau$, and an overall intensity factor $K$. We minimize the merit function $\chi^2$, defined as the sum of square errors normalized by the error bars on the data points. These error bars are due to the photon noise, which goes as the square root of the number of counts. We chose a constant value for $c_\infty = 3{,}000$ m s$^{-1}$ (44); we checked that the results are not sensitive to this choice. All fits are very good, with a reduced $\chi^2$ between 0.83 and 2.0, with an average of 1.28. To illustrate the quality of the fit, we show in Fig. S1 the residuals of the fits to the spectra displayed in Fig. 2*B*; they are compatible with the photon noise. The maximum value found for $\tau$ is 18 ps: our experiments are in the regime where relaxation effects are small, with $(c/c_\infty)^4(\omega\tau)^2 \ll 1$ (0.03 at most).

**Molecular Dynamics Simulations.** We have performed molecular dynamics simulations of $c$ at the same thermodynamic conditions as the experiments. We simulate a system of N = 500 water molecules interacting by means of TIP4P/2005 (31) with periodic boundary conditions. TIP4P/2005 represents water as a rigid and nonpolarizable molecule. It consists of a Lennard-Jones site centered at the oxygen atom and a Coulomb interaction given by two partial charges placed at the hydrogen atom and a negative one placed at a point M along the bisector of the HOH angle. A schematic representation of the model is presented in Fig. S2.

The parametrization of TIP4P/2005 has been based on a fit of the temperature of maximum density and a great variety of properties and wide range thereof for the liquid and its polymorphs. TIP4P/2005 has been used to calculate a broad variety of thermodynamic properties of the liquid and solid phases, such as the phase diagram involving condensed phases (45–47), properties at melting and vaporization (34, 48), dielectric constants (49), pair distribution function, and self-diffusion coefficient. These properties cover a temperature range from 123 to 573 K and pressures up to 4,000 MPa (32). We have performed molecular dynamics simulations with the GROMACS 4.5 package (50, 51) using the particle mesh Ewald method (52) to calculate the long-range electrostatics forces and the LINCS algorithm (53) to constrain the intramolecular degrees of freedom. We set the time step to 0.5 fs and make use of the velocity-rescaling thermostat (54) and the Parrinello–Rahman barostat (55), with coupling constants set to 1 and 2 ps, respectively. The Lennard-Jones interactions are truncated at 9.5 Å. The contributions to the energy and pressure beyond this distance are approximated assuming that the molecules are uniformly distributed. To calculate the sound velocity of supercooled TIP4P/2005 water at negative pressure, the simulated times vary between 40 and 150 ns (at the lowest temperatures). The increased length of the runs at the lowest temperatures is due to the amplified density–energy fluctuations in this region for TIP4P/2005 [and other models as well (56)]. This leads to an increase of the error bar associated with the calculated quantities at the lower temperatures.

The sound velocity $c$ is defined by the Newton–Laplace formula:

$$c = \sqrt{\frac{1}{\rho\kappa_S}} = \sqrt{\frac{C_p}{C_V}\frac{1}{\rho\kappa_T}}, \quad [3]$$

where $\rho$ is the density, $\kappa_S = -(1/V)(\partial V/\partial p)_S$, and $\kappa_T = -(1/V)(\partial V/\partial p)_T$ are the adiabatic and isothermal compressibility, respectively, defined in terms of the entropy $S$, volume $V$, pressure $p$, and temperature $T$ of the system. $C_p$ and $C_v$ are the heat capacity at constant pressure and volume, respectively. We calculate $C_V$, $C_p$, and $\kappa_T$ using the fluctuation formulas,

$$C_V = \frac{\langle U^2\rangle - \langle U\rangle^2}{k_B T^2}, \quad C_p = \frac{\langle H^2\rangle - \langle H\rangle^2}{k_B T^2}, \quad \kappa_T = \frac{\langle V^2\rangle - \langle V\rangle^2}{\langle V\rangle k_B T}, \quad [4]$$

where $U$ is the energy, $H$ the enthalpy, and $k_B$ the Boltzmann constant. We run numerical simulations in two different ensembles. First, by equilibrating the system in a canonical (*NVT*) ensemble, we compute $C_V$. Next, by equilibrating the system an isothermal-isobaric ensemble (*NpT*), we compute $C_p$ and $\kappa_T$ for a system of N = 500 water molecules.

We have also used an alternative method to obtain $C_V$, coming back to its definition:

$$C_V = \left(\frac{\delta U}{\delta T}\right)_V. \quad [5]$$

Thus, we compute the values of the energy along the desired isochore and calculate $C_V$ as the derivative with respect to $T$. Table S3 shows the consistency between the values obtained with each route.

**ACKNOWLEDGMENTS.** We thank C. Austen Angell and José Teixeira for discussions; Véronique Gardien for providing us with sample 2; and Abraham D. Stroock and Carlos Vega for suggestions to improve the manuscript. The team at Lyon acknowledges funding by the European Research Council under the European Community's FP7 Grant Agreement 240113, and by the Agence Nationale de la Recherche Grant 09-BLAN-0404-01. C.V. acknowledges financial support from a Marie Curie Integration Grant PCIG-GA-2011-303941 and thanks the Ministerio de Educacion y Ciencia and the

Universidad Complutense de Madrid for a Juan de la Cierva Fellowship. The team at Madrid acknowledges funding from the Ministerio de ciencia e innovación (MCINN) Grant FIS2013-43209-P. The team at Madrid acknowledges the use of the supercomputational facility Minotauro from the Spanish Supercomputing Network (RES), along with the technical support (through project QCM-2014-1-0038).

1. Speedy RJ, Angell CA (1976) Isothermal compressibility of supercooled water and evidence for a thermodynamic singularity at -45°C. *J Chem Phys* 65(3):851–858.
2. Speedy RJ (1982) Stability-limit conjecture. An interpretation of the properties of water. *J Phys Chem* 86(6):982–991.
3. The International Association for the Properties of Water and Steam (2009) Revised release on the IAPWS formulation 1995 for the thermodynamic properties of ordinary water substance for general and scientific use. Available at www.iapws.org/relguide/IAPWS-95.html. Accessed October 20, 2013.
4. Poole PH, Sciortino F, Essmann U, Stanley HE (1992) Phase behaviour of metastable water. *Nature* 360(6402):324–328.
5. Sciortino F, Poole PH, Essmann U, Stanley HE (1997) Line of compressibility maxima in the phase diagram of supercooled water. *Phys Rev E Stat Phys Plasmas Fluids Relat Interdiscip Topics* 55(1):727–737.
6. Xu L, et al. (2005) Relation between the Widom line and the dynamic crossover in systems with a liquid-liquid phase transition. *Proc Natl Acad Sci USA* 102(46):16558–16562.
7. El Mekki Azouzi M, Ramboz C, Lenain J-F, Caupin F (2013) A coherent picture of water at extreme negative pressure. *Nat Phys* 9(1):38–41.
8. Debenedetti PG (2003) Supercooled and glassy water. *J Phys Condens Matter* 15(45): R1669–R1726.
9. Poole PH, Sciortino F, Grande T, Stanley HE, Angell CA (1994) Effect of hydrogen bonds on the thermodynamic behavior of liquid water. *Phys Rev Lett* 73(12): 1632–1635.
10. Zheng Q, et al. (2002) *Liquids Under Negative Pressure, NATO Science Series II*, eds Imre AR, Maris HJ, Williams PR (Kluwer Academic Publishers, Dordrecht, The Netherlands), Vol 84, pp 33–46.
11. Angell CA (2008) Insights into phases of liquid water from study of its unusual glass-forming properties. *Science* 319(5863):582–587.
12. Sastry S, Debenedetti PG, Sciortino F, Stanley HE (1996) Singularity-free interpretation of the thermodynamics of supercooled water. *Phys Rev E Stat Phys Plasmas Fluids Relat Interdiscip Topics* 53(6):6144–6154.
13. Stokely K, Mazza MG, Stanley HE, Franzese G (2010) Effect of hydrogen bond cooperativity on the behavior of water. *Proc Natl Acad Sci USA* 107(4):1301–1306.
14. Liu D, et al. (2007) Observation of the density minimum in deeply supercooled confined water. *Proc Natl Acad Sci USA* 104(23):9570–9574.
15. Murata K-I, Tanaka H (2012) Liquid-liquid transition without macroscopic phase separation in a water-glycerol mixture. *Nat Mater* 11(5):436–443.
16. Caupin F, Herbert E (2006) Cavitation in water: A review. *C R Phys* 7(9-10):1000–1017.
17. Caupin F, Stroock AD (2013) The stability limit and other open questions on water at negative pressure. *Liquid Polymorphism: Advances in Chemical Physics*, ed Stanley HE (Wiley, New York), Vol 152, pp 51–80.
18. Zheng Q, Durben DJ, Wolf GH, Angell CA (1991) Liquids at large negative pressures: Water at the homogeneous nucleation limit. *Science* 254(5033):829–832.
19. Alvarenga AD, Grimsditch M, Bodnar RJ (1993) Elastic properties of water under negative pressures. *J Chem Phys* 98(11):8392–8396.
20. Shmulovich KI, Mercury L, Thiéry R, Ramboz C, El Mekki M (2009) Experimental superheating of water and aqueous solutions. *Geochim Cosmochim Acta* 73(9):2457–2470.
21. Henderson S, Speedy R (1980) A Berthelot-Bourdon tube method for studying water under tension. *J Phys E Sci Instrum* 13:778–782.
22. Teixeira J, Leblond J (1978) Brillouin scattering from supercooled water. *J. Physique Lett* 39(7):83–85.
23. Conde O, Leblond J, Teixeira J (1980) Analysis of the dispersion of the sound velocity in supercooled water. *J Phys* 41(9):997–1000.
24. Conde O, Teixeira J, Papon P (1982) Analysis of sound velocity in supercooled H2O, D2O, and water-ethanol mixtures. *J Chem Phys* 76(7):3747–3753.
25. Maisano G, et al. (1984) Evidence of anomalous acoustic behavior from Brillouin scattering in supercooled water. *Phys Rev Lett* 52(12):1025–1028.
26. Magazu S, et al. (1989) Relaxation process in deeply supercooled water by Mandelstam-Brillouin scattering. *J Phys Chem* 93(2):942–947.
27. Cunsolo A, Nardone M (1996) Velocity dispersion and viscous relaxation in supercooled water. *J Chem Phys* 105(10):3911–3917.
28. Davitt K, Rolley E, Caupin F, Arvengas A, Balibar S (2010) Equation of state of water under negative pressure. *J Chem Phys* 133(17):174507.
29. Netz PA, Starr FW, Stanley HE, Barbosa MC (2001) Static and dynamic properties of stretched water. *J Chem Phys* 115(1):344–348.
30. Yamada M, Mossa S, Stanley HE, Sciortino F (2002) Interplay between time-temperature transformation and the liquid-liquid phase transition in water. *Phys Rev Lett* 88(19):195701.
31. Abascal JLF, Vega C (2005) A general purpose model for the condensed phases of water: TIP4P/2005. *J Chem Phys* 123(23):234505.
32. Vega C, Abascal JLF (2011) Simulating water with rigid non-polarizable models: A general perspective. *Phys Chem Chem Phys* 13(44):19663–19688.
33. Abascal JLF, Vega C (2011) Note: Equation of state and compressibility of supercooled water: Simulations and experiment. *J Chem Phys* 134(18):186101.
34. Vega C, Abascal JLF, Nezbeda I (2006) Vapor-liquid equilibria from the triple point up to the critical point for the new generation of TIP4P-like models: TIP4P/Ew, TIP4P/2005, and TIP4P/ice. *J Chem Phys* 125(3):34503.
35. Hare DE, Sorensen CM (1987) The density of supercooled water. II. Bulk samples cooled to the homogeneous nucleation limit. *J Chem Phys* 87(8):4840–4845.
36. Ohmori T, Kimura Y, Hirota N, Terazima M (2001) Thermal diffusivities and sound velocities of supercritical methanol and ethanol measured by the transient grating method. *Phys Chem Chem Phys* 3(18):3994–4000.
37. Abascal JLF, Vega C (2010) Widom line and the liquid-liquid critical point for the TIP4P/2005 water model. *J Chem Phys* 133(23):234502.
38. Limmer DT, Chandler D (2013) The putative liquid-liquid transition is a liquid-solid transition in atomistic models of water. II. *J Chem Phys* 138(21):214504.
39. Kanno H, Speedy RJ, Angell CA (1975) Supercooling of water to -92°C under pressure. *Science* 189(4206):880–881.
40. Mishima O, Stanley HE (1998) The relationship between liquid, supercooled and glassy water. *Nature* 396(6709):329–335.
41. The International Association for the Properties of Water and Steam (1992) Revised supplementary release: Saturation properties of ordinary water substance, September 1992. Available at http://www.iapws.org/relguide/supsat.pdf. Accessed October 20, 2013.
42. Boon JP, Yip S (1980) *Molecular Hydrodynamics* (McGraw-Hill, New York).
43. The International Association for the Properties of Water and Steam (1997) Release on the refractive index of ordinary water substance as a function of wavelength, temperature and pressure. Available at http://www.iapws.org/relguide/rindex.pdf. Accessed October 20, 2013.
44. Bencivenga F, Cimatoribus A, Gessini A, Izzo MG, Masciovecchio C (2009) Temperature and density dependence of the structural relaxation time in water by inelastic ultraviolet scattering. *J Chem Phys* 131(14):144502.
45. Aragones JL, Vega C (2009) Plastic crystal phases of simple water models. *J Chem Phys* 130(24):244504.
46. Conde MM, Vega C, Tribello GA, Slater B (2009) The phase diagram of water at negative pressures: Virtual ices. *J Chem Phys* 131(3):034510.
47. Aragones JL, MacDowell LG, Siepmann JI, Vega C (2011) Phase diagram of water under an applied electric field. *Phys Rev Lett* 107(15):155702.
48. Vega C, Abascal JLF, Conde MM, Aragones JL (2009) What ice can teach us about water interactions: A critical comparison of the performance of different water models. *Faraday Discuss* 141:251–276, discussion 309–346.
49. Aragones JL, MacDowell LG, Vega C (2011) Dielectric constant of ices and water: A lesson about water interactions. *J Phys Chem A* 115(23):5745–5758.
50. Hess B, Kutzner C, van der Spoel D, Lindahl E (2008) GROMACS 4: Algorithms for highly efficient, load-balanced, and scalable molecular simulation. *J Chem Theory Comput* 4(3):435–447.
51. Van Der Spoel D, et al. (2005) GROMACS: Fast, flexible, and free. *J Comput Chem* 26(16):1701–1718.
52. Essmann U, et al. (1995) A smooth particle mesh Ewald method. *J Chem Phys* 103(19): 8577–8593.
53. Hess B (2008) P-LINCS: A parallel linear constraint solver for molecular simulation. *J Chem Theory Comput* 4(1):116–122.
54. Bussi G, Donadio D, Parrinello M (2007) Canonical sampling through velocity rescaling. *J Chem Phys* 126(1):014101.
55. Parrinello M, Rahman A (1981) Polymorphic transitions in single crystals: A new molecular dynamics method. *J Appl Phys* 52(12):7182–7190.
56. Shevchuk R, Rao F (2012) Note: Microsecond long atomistic simulation of supercooled water. *J Chem Phys* 137(3):036101.

# Supporting Information

Pallares et al. 10.1073/pnas.1323366111

## SI Text

**Data Analysis and Error Bars.** When the experimental spectra were fitted with the function given by Eq. **2**, convoluted with the instrumental resolution function (IRF) and corrected for the dark count, the results for sample 1 with a bubble present exhibited a sound velocity value systematically lower than the reference data for liquid water in equilibrium with its vapor (1–3). This is due to the uncertainty in the $\lambda$, and to the finite numerical aperture of the objective (0.70) (4). The average scattering angle $2\theta$ is less than 180°, which lowers the value of $Q = 4\pi n \sin\theta/\lambda$. The results for the sound velocity must be corrected for this effect: a uniform factor of 1.0086 (which corresponds to $2\theta = 165°$, compatible with the numerical aperture of the objective) is sufficient to bring the data for sample 1 with a bubble present in excellent agreement with the reference data. Fig. S3 shows the residuals. Their SD was used to set the error bar, which gave 6 m $s^{-1}$ (less than 0.45%) and was applied to all data.

The guides to the eye in Fig. 3*A* are arbitrary fits to the data for the homogenized samples. With the 6-m $s^{-1}$ error bar, the resulting reduced $\chi^2$ is 0.94 and 1.98 for samples 1 and 2, respectively, showing that the data scatter is compatible with the error bar. Note that the measurements were performed over a 1-mo period, with many thermal cyclings of the samples, and also indifferently after heating or cooling. This illustrates the reproducibility of the results. We have also performed repeated measurements under the same conditions on a sample similar to sample 2, but containing salty water. We gathered five measurements at −10°C and four measurements at −15°C. The relative SD of the sound velocity for each group of data is 4.6 and 3.5 m $s^{-1}$, respectively, which is even less than the 6 m $s^{-1}$ used for the error bar. The uncertainty given by the nonlinear fitting procedure on the sound velocity is also always less than 6 m $s^{-1}$, except for three of the four lower temperature points for sample 2. These exceptions come from a low number of photon counts in the corresponding spectra, due in particular to the extremely small size of sample 2. For these points (for which the reduced $\chi^2$ of the fit remains less than 2), the 6-m $s^{-1}$ error bar was replaced by the uncertainty on the fit parameter, which amounted to at most 7.8 m $s^{-1}$.

Finally, we discuss the statistical confidence we can have about the minimum in sound velocity versus temperature along the isochore at $\rho_1$. The data points at the six lowest temperatures are in an order such that the sound velocity decreases with increasing temperature. At higher temperature it clearly increases with temperature. Can this be due to a statistical fluctuations of the measured values? The limiting case would be that the sound velocity reaches a plateau. Hence an attempt was made to fit the data at the six lowest temperatures with a constant (Fig. S4).

The fit gives 1,320 m $s^{-1}$, but an unreasonably high reduced $\chi^2 = 4.55$. To check the significance of this value, we have simulated $2^{20} = 1{,}048{,}576$ series of 6 points, picked up from a Gaussian distribution with mean value 1,320 m $s^{-1}$ and SD 6 m $s^{-1}$. Only in 453 occurrences (0.043%) does the reduced $\chi^2$ exceed 4.5. Only in 1,450 occurrences (0.14%) are the six data in descending order, and among these, only one has a reduced $\chi^2$ above 4.5. We conclude that the minimum in sound velocity versus temperature along the isochore at $\rho_1$ is observed with more than 99.8% confidence.

**International Association for the Properties of Water and Steam Equation of State.** The International Association for the Properties of Water and Steam (IAPWS) provides useful releases on the properties of water for general and scientific use. The equation of state is given by a multiparameter formulation for the Helmholtz free energy (1, 2). The Helmholtz free energy is separated into two parts, an ideal-gas part and a residual part. The latter is fitted to a comprehensive set of experimental data (thermal properties of the single-phase region and of the vapor–liquid phase boundary, specific isochoric heat capacity, specific isobaric heat capacity, speed of sound, differences in the specific enthalpy and in the specific internal energy, Joule–Thomson coefficient, and isothermal throttling coefficient). It is stated (1) that this formulation is "valid in the entire stable fluid region of $H_2O$ from the melting-pressure curve to 1,273 K at pressures up to 1,000 MPa," and that it "represents the currently available experimental data of the subcooled liquid (solid-liquid metastable region) and of the superheated liquid (liquid-gas metastable region) to within the experimental uncertainty." The sound velocity can be computed using appropriate derivatives. A comparison showing the agreement between the calculated sound velocity and experimental data on supercooled water at ambient pressure is given in figure 7 of ref. 5. The saturation properties of water, including the density along the liquid–vapor binodal, are also available (3).

**Water Purity.** Water in natural and synthetic fluid inclusions may contain salt (6, 7), although Raman scattering studies show that fluid inclusions can be synthesized with a negligible salt content (7, 8). Dissolved salts will lower the melting point of the frozen samples. It has been shown (6) that the measurement of the melting point depression gives a value for the salt content consistent with the value obtained using Raman scattering from the liquid. Water in samples 1 and 2 melt at 0.1°C and 0.3°C, respectively, which is consistent with pure water given the uncertainty of the stage (0.15°C) and the difficulty to detect changes of phase in sample 2 due to its small size. We also note that water in our simulations is pure, and gives results consistent with our measurements; it would be surprising that this is the case if samples 1 and 2 contained impure water. As a further test of water purity, we have measured the sound velocity in fluid inclusions as a function of temperature when a bubble is present. Fig. S5 compares the results with our measurements on a simple ultrapure (Millipore Direct Q3 UV) free water droplet and with literature data. All results agree within the error bars. Fig. S5 also displays the sound velocity along the binodal for several aqueous NaCl solutions. They are clearly higher than the measured values. Taking the error bars into account, we conclude that water in the inclusions studied has a purity greater than 99.8 mol %, even higher than the samples studied in ref. 7.

**Discussion of Possible Artifacts.** In this section, we consider other possible explanations of the experimental results.

First, we question the validity of the isochoric assumption. In platelet-like inclusions, Alvarenga et al. (8) have shown that the inclusion walls could collapse when submitted to large tensions, thus increasing the density in comparison with the isochore. However, our inclusions are not platelet-like and a simple density effect could not explain the values of sound velocity above the binodal observed at low temperature. Indeed, the density cannot become higher than the binodal, because the inclusion would then experience positive pressures, and any deformation would yield densities lower than the isochore density.

One could also argue that a phase transition occurs inside the inclusion. If the newly formed phase had a low density, the density of the liquid in equilibrium would increase, thus yielding

a sound velocity larger than expected. At the given thermodynamics conditions, the most natural candidate for the newly formed phase would be hexagonal ice. However, at $-12^{\circ}$C, the ice–liquid equilibrium occurs at $+128$ MPa and the sound velocity of the liquid would be around 1,575 m s$^{-1}$ (2), much higher than the largest measured value, 1,414 m s$^{-1}$ for sample 2. To get a lower sound velocity for the liquid, one should think of a newly formed phase having higher density than hexagonal ice. This also excludes cubic ice, the only other crystal that could be found in this region of the phase diagram. Therefore, one could recur to another liquid phase, which would appear if we had actually crossed a liquid–liquid transition (LLT). This would require the LLT to be at negative pressure, which has been already found in a few simulations (9–11) (see however ref. 12) and proposed for some models (13, 14). However, in our experimental measurements, we did not see the two other Brillouin peaks that would come from the low-density liquid, and we did not find any hysteresis between measurements taken after heating or cooling. A possibility remains that the Brillouin shifts of the two liquids are too close to be seen with the resolution of our setup. However, another difficulty arises: To explain why the sound velocity in both samples rises above the binodal, one would require the LLT to lie at positive pressure at $-12$°C. Undoubtedly, this should have been seen in the numerous experiments performed in this region. Therefore, the hypothesis suggesting that a phase transition occurred also has to be discarded.

**On the Origin of a Minimum in the Sound Velocity.** The simulations enable a detailed analysis of the appearance of a minimum in the sound velocity. In Fig. S6 we represent the values of the adiabatic index $\gamma$ and of the isothermal compressibility $\kappa_T$.

Both quantities show an extremum, a minimum for $\gamma$ and a maximum for $\kappa_T$. Because the sound velocity depends inversely on the latter (Eq. **3**), both $\gamma$ and $\kappa_T$ justify the minimum in the sound velocity. However, the relative variation of the isothermal compressibility along the isochores is sensibly larger than that of the adiabatic index. Thus, $\kappa_T$ mostly determines the appearance of the minimum in $c$. Note that, however, below $\simeq -100$ MPa, $\kappa_T$ becomes monotonic along isobars. A minimum is still seen in the temperature variation of the sound velocity for sample 1 because the variation is taken along an isochore (Fig. S6).

**Calculation of the Pressure.** To compute the pressure, we equilibrate the system at fixed values of $N$, $V$, and $T$, and use the virial expression. Because our TIP4P/2005 simulations and our sound velocity measurements agree well for both isochores studied, the pressure calculated in the simulations gives a reasonable estimate of the actual pressure reached in the samples. Fig. S7 shows the pressure as a function of temperature along the two isochores $\rho_1$ and $\rho_2$ and the binodal.

The values of the pressure and temperature along isochore $\rho_1$ are represented in Table S1 and along isochore $\rho_2$ in Table S2.


1. Wagner W (2002) The IAPWS formulation 1995 for the thermodynamic properties of ordinary water substance for general and scientific use. *J Phys Chem Ref Data* 31(2):387–535.
2. The International Association for the Properties of Water and Steam (2009) Revised release on the IAPWS formulation 1995 for the thermodynamic properties of ordinary water substance for general and scientific use. Available at www.iapws.org/relguide/IAPWS-95.html. Accessed October 20, 2013.
3. The International Association for the Properties of Water and Steam (1992) Revised supplementary release: Saturation properties of ordinary water substance, September 1992. Available at http://www.iapws.org/relguide/supsat.pdf. Last accessed October 20, 2013.
4. Bencivenga F, et al. (2012) A high resolution ultraviolet Brillouin scattering set-up. *Rev Sci Instrum* 83(10):103102.
5. Holten V, Bertrand CE, Anisimov MA, Sengers JV (2012) Thermodynamics of supercooled water. *J Chem Phys* 136(9):094507.
6. Green JL, Durben DJ, Wolf GH, Angell CA (1990) Water and solutions at negative pressure: Raman spectroscopic study to -80 megapascals. *Science* 249(4969):649–652.
7. Zheng Q, Durben DJ, Wolf GH, Angell CA (1991) Liquids at large negative pressures: water at the homogeneous nucleation limit. *Science* 254(5033):829–832.
8. Alvarenga AD, Grimsditch M, Bodnar RJ (1993) Elastic properties of water under negative pressures. *J Chem Phys* 98(11):8392–8396.
9. Tanaka H (1996) Phase behaviors of supercooled water: Reconciling a critical point of amorphous ices with spinodal instability. *J Chem Phys* 105(12):5099–5111.
10. Brovchenko I, Geiger A, Oleinikova A (2005) Liquid-liquid phase transitions in supercooled water studied by computer simulations of various water models. *J Chem Phys* 123(4):044515.
11. Brovchenko I, Oleinikova A (2008) Multiple phases of liquid water. *ChemPhysChem* 9(18):2660–2675.
12. Liu Y, Panagiotopoulos AZ, Debenedetti PG (2009) Low-temperature fluid-phase behavior of ST2 water. *J Chem Phys* 131(10):104508.
13. Angell CA (2008) Insights into phases of liquid water from study of its unusual glass-forming properties. *Science* 319(5863):582–587.
14. Stokely K, Mazza MG, Stanley HE, Franzese G (2010) Effect of hydrogen bond cooperativity on the behavior of water. *Proc Natl Acad Sci USA* 107(4):1301–1306.
15. Chen C-T, Chen L-S, Millero FJ (1978) Speed of sound in NaCl, $MgCl_2$, $Na_2SO_4$, and $MgSO_4$ aqueous solutions as functions of concentration, temperature, and pressure. *J Acoust Soc Am* 63(6):1795–1800.


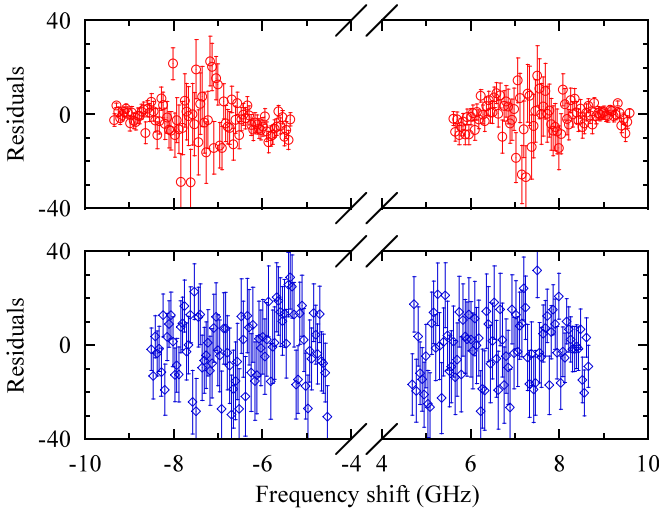


**Fig. S1.** Residuals of the fits based on Eq. **2** to the experimental spectra shown in Fig. 2*B* for homogenized sample 1 at 140°C (*Upper*) and −12°C (*Lower*). The error bars are the square root of the photon counts at each frequency. The data for −12°C were not rescaled (in contrast with Fig. 2*B*).

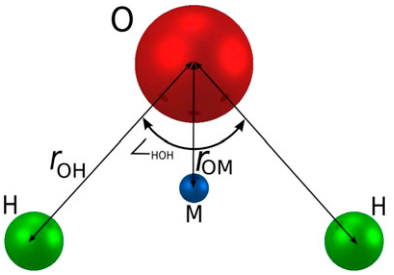


**Fig. S2.** Schematic representation of the four-site model of water TIP4P/2005, consisting of a Lennard-Jones center at the oxygen atom (in red) and three charged sites: two positive charges at the hydrogen atoms and a compensating negative charge at a dummy atom (labeled as M) placed near the oxygen along the bisector of the HOH angle.

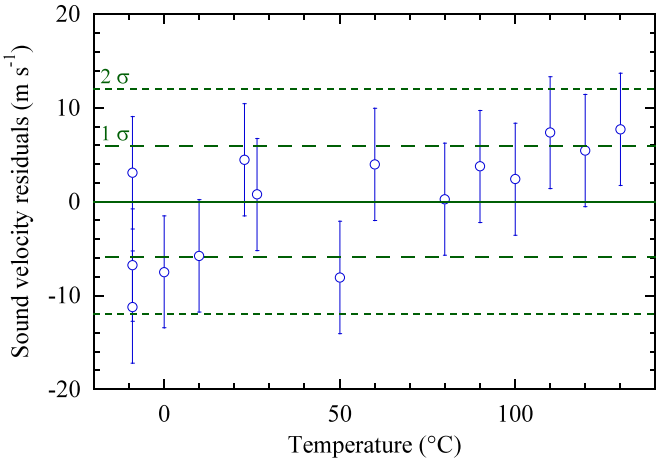


**Fig. S3.** Sound velocity residuals of the data for sample 1 with a bubble present, to the reference data for liquid water in equilibrium with its vapor (1–3). Their SD $\sigma = 5.97$ m s$^{-1}$ was used to set the error bar on the sound velocity to 6 m s$^{-1}$.

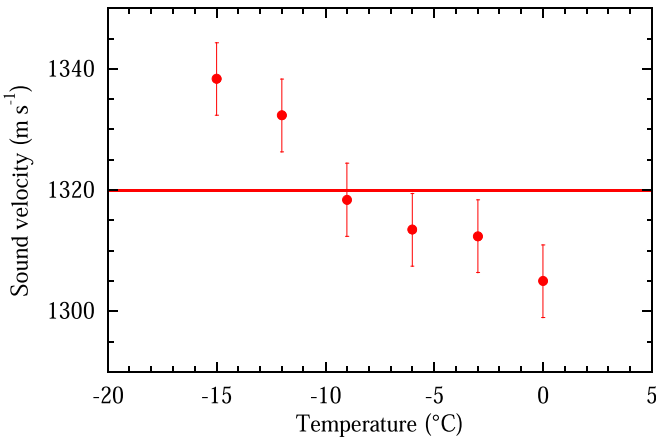


**Fig. S4.** Sound velocity at low temperature for the homogenized sample 1. The red line is an attempt to fit the data with a constant. It yields $c = 1{,}320$ m s$^{-1}$, but an unreasonably high reduced $\chi^2 = 4.55$.

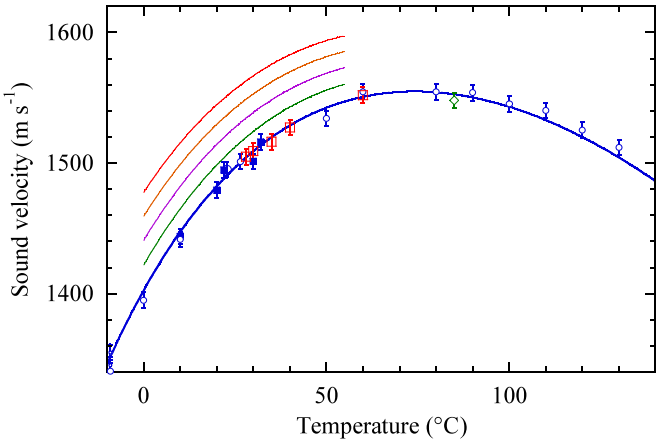


**Fig. S5.** Sound velocity versus temperature along the liquid–vapor equilibrium. The symbols show our Brillouin measurements for sample 1 (open blue circles), sample 2 (open green diamond), another fluid inclusion from the same quartz crystal as sample 2 (open red squares), and an ultrapure (Millipore Direct Q3 UV) water droplet deposited on glass slide (filled blue squares). The three symbol sizes correspond to three pinhole sizes on the spectrometer. The blue curve is the literature value for pure water (1–3), and the other curves illustrate the shift in sound velocity due to dissolved NaCl, measured at 0.1 MPa (ref. 15). The salt molality increases from bottom to top: 0.25 (green), 0.5 (purple), 0.75 (brown), and 1 (red).

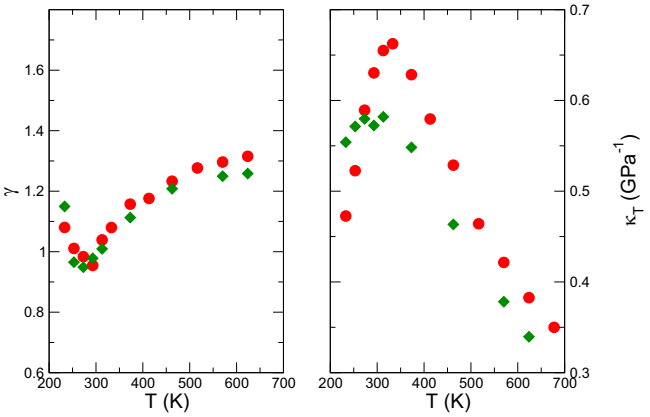


**Fig. S6.** Contributions of the adiabatic index (*Left*) and the isothermal compressibility (*Right*) to the sound velocity along the isochores at $\rho_1 = 933.2$ kg m$^{-3}$ (red circles) and $\rho_2 = 952.5$ kg m$^{-3}$ (green diamonds).

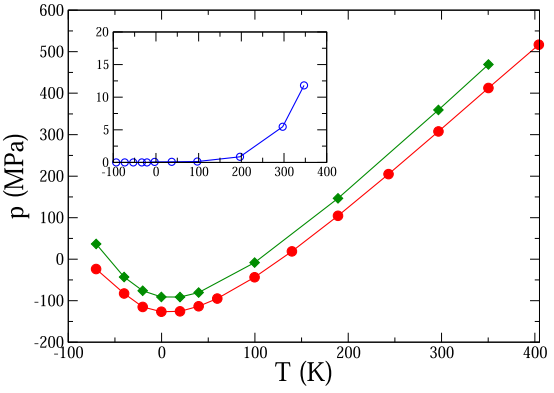


**Fig. S7.** Pressure versus temperature for the isochores at $\rho_1$ (red circles) and $\rho_2$ (green diamonds) and the binodal (open blue circles, *Inset*).

**Table S1. Pressure versus temperature for the isochore $\rho_1$**

| $T$, K | Pressure, MPa | $T$, K | Pressure, MPa |
|---|---|---|---|
| 202.99 | −23.7 | 372.82 | −43.5 |
| 232.99 | −82.7 | 412.82 | 18.8 |
| 252.90 | −115.0 | 462.19 | 104.6 |
| 272.90 | −126.5 | 516.37 | 205.0 |
| 292.87 | −125.6 | 569.85 | 307.8 |
| 312.87 | −113.5 | 623.41 | 412.5 |
| 332.85 | −94.9 | 677.41 | 516.8 |

**Table S2. Pressure versus temperature for the isochore $\rho_2$**

| $T$, K | Pressure, MPa | $T$, K | Pressure, MPa |
|---|---|---|---|
| 203.01 | 36.7 | 312.88 | −80.4 |
| 233.01 | −43.0 | 372.85 | −8.2 |
| 252.91 | −76.0 | 462.19 | 146.6 |
| 272.90 | −91.0 | 569.84 | 359.6 |
| 292.89 | −91.2 | 623.41 | 469.2 |

**Table S3. Values of $C_v$ for the isochore $\rho = 933.2$ kg m$^{-3}$ obtained with the energy fluctuations formula (Eq. 4, second column) and the thermodynamic definition (Eq. 5, third column)**

| $T$, K | $C_V$, Eq. **4** | $C_V$, Eq. **5** |
|---|---|---|
| 203 | 122 ± 6 | 119 |
| 233 | 110 ± 10 | 111 |
| 253 | 115 ± 10 | 105 |
| 273 | 114 ± 10 | 100 |
| 293 | 105 ± 5 | 95.0 |
| 313 | 93.5 ± 5 | 90.3 |
| 333 | 85.3 ± 4 | 85.9 |
| 373 | 75.3 ± 4 | 77.8 |
| 413 | 70.1 ± 3 | 70.7 |
| 462 | 63.2 ± 3 | 63.3 |
| 516 | 58.5 ± 3 | 57.0 |
| 570 | 55.0 ± 3 | 52.6 |
| 623 | 52.5 ± 3 | 50.1 |

Results are given in J K$^{-1}$ mol$^{-1}$.